Editors' Suggestion

Impact of grain boundary energy anisotropy on grain growth

S. Kiana Naghibzadeh,[1,*] Zipeng Xu,[2] David Kinderlehrer,[3] Robert Suter,[4,2] Kaushik Dayal,[5,3,6] and Gregory S. Rohrer[2]

[1]*Department of Civil and Environmental Engineering, Massachusetts Institute of Technology, Cambridge, Massachusetts 02139, USA*
[2]*Department of Materials Science and Engineering, Carnegie Mellon University, Pittsburgh, Pennsylvania 15213, USA*
[3]*Center for Nonlinear Analysis, Department of Mathematical Sciences, Carnegie Mellon University, Pittsburgh, Pennsylvania 15213, USA*
[4]*Department of Physics, Carnegie Mellon University, Pittsburgh, Pennsylvania 15213, USA*
[5]*Department of Civil and Environmental Engineering, Carnegie Mellon University, Pittsburgh, Pennsylvania 15213, USA*
[6]*Department of Mechanical Engineering, Carnegie Mellon University, Pittsburgh, Pennsylvania 15213, USA*

(Received 29 April 2024; accepted 30 August 2024; published 19 September 2024)

A threshold dynamics model of grain growth that accounts for the anisotropy in the grain boundary energy has been used to simulate experimentally observed grain growth of polycrystalline Ni. The simulation reproduces several aspects of the observed microstructural evolution that are not found in the results of simulations assuming isotropic properties. For example, the relative areas of the lowest-energy twin boundaries increase as the grains grow and the average grain boundary energy decreases with grain growth. This decrease in energy occurs because the population of higher-energy grain boundaries decreases while the population of lower-energy boundaries increases as the total grain boundary area decreases. This phenomenon emerges from the assumption of anisotropic grain boundary energies without modification of the energy minimizing algorithm. These findings are consistent with the observation that, in addition to the decrease in grain boundary area, additional energy is dissipated during grain growth by a decrease in the average grain boundary energy.

DOI: 10.1103/PhysRevMaterials.8.093403

I. INTRODUCTION

Grain boundaries are the interfaces between crystals with different lattice orientations in polycrystalline metals, ceramics, polymers, and rocks. At high temperatures, grain boundaries migrate and this is one important mechanism for the evolution of polycrystalline microstructures. Grain growth, which is an increase in the average crystal size by grain boundary migration, affects structure-sensitive material properties. Hence, understanding the underlying mechanism of grain boundary migration is necessary for controlling the electrical, optical, and mechanical properties of materials. Grain growth by grain boundary migration has been extensively studied in the past using analytical theories [1–3], molecular dynamics simulations [4–11], Monte Carlo simulations [12–14], phase field simulations [15–29], threshold dynamics [30,31] and other approaches [32–41].

Recent experimental observations have provided two findings not captured by most of the simulations. The first is that grain boundaries are approximately equally likely to migrate toward or away from their centers of curvature [42–44]. The second is that while grain boundaries move to decrease the total energy of the system by decreasing the grain boundary area, they further decrease the energy by replacing high-energy grain boundaries with low-energy ones, a process referred to as grain boundary replacement [45]. This suggests that grain boundary energy must be included in the simulations. The grain boundary energy (GBE) depends on five macroscopic parameters, which can be expressed as the lattice misorientation between the two adjacent grains (three degrees of freedom) forming the boundary, and the orientation of the boundary plane (two degrees of freedom) [46,47]. However, most previous grain growth simulations considered isotropic grain boundary energy, i.e., the energy is the same for all boundaries, and this cannot capture the replacement of high-energy grain boundaries with low-energy ones.

Most of the simulations that used anisotropic properties only considered the dependency of GBE on the misorientation [48–50] or simulated grain growth in two dimensions [36]. However, the GBE varies more strongly with variations in the grain boundary plane orientation than with the lattice misorientation [47], so it seems unlikely that simulations ignoring these parameters will correctly simulate the energy reduction during grain growth.

Two prior examples of three-dimensional simulations considering the grain boundary plane dependence on the GBE in three-dimensions considered a hypothetical GBE function and did not include the dependence of the GBE on the lattice misorientation [38,51]. A limited number of recent studies have simulated grain growth in 3D using a GBE that varies with all five parameters [30,52,53]. Kim *et al.* [53] used the phase field method to simulate grain growth in BCC Fe and found that the anisotropic GBE influenced the morphological evolution of grains and that low-energy boundaries increased in population during grain growth. Hallberg and Bulatov [52] developed an anisotropic level set method to show the importance of energy anisotropy in the morphology of evolved

*Contact author: kiana@mit.edu

microstructures. The simulations used energies specified by the Bulatov-Reed-Kumar (BRK) energy function [54] for fcc structures and models no more than four grains. Nino and Johnson [30] used a simplified extension of threshold dynamics (TD) with different energy functions to study the effect of energy anisotropy on the evolution of a microstructure instantiated with a Voronoi tessellation. This simplified version employed Gaussian kernels to describe the GBE of boundaries of different inclinations. A discussion on the difference between the current method and an extension used by [30] is provided in Sec. II A.

The purpose of this study was to compare the outcome of the simulated 3D microstructure evolution with the experimentally observed evolution of Ni during grain growth [55,56] using both an isotropic and a five-parameter anisotropic GBE. The simulations described here differ from the previous study in two ways. The first is that an improved description of the grain boundary energy anisotropy, described in Sec. II A, is implemented. The second is that experimentally observed microstructures are used as input, and the results are compared to the observed microstructure in later states. The experimentally determined starting microstructures contain 2400 to 3000 grains, and we quantify changes in the average grain boundary energy and the grain boundary energy distribution, the grain boundary area, the grain boundary curvature, the grain boundary velocity, changes in the numbers of near neighbors, and the relative areas of twin boundaries. The simulation captures the replacement of higher energy GBs by lower energy boundaries in the same manner that was observed experimentally [45], while the isotropic simulation cannot necessarily predict this mechanism.

To simulate grain growth, we have used the TD method originally introduced by Merriman, Bence, and Osher in [57,58] which uses an implicit representation of boundaries. There are three reasons for choosing the TD method. The first is the high computational efficiency compared to other methods using an implicit representation of the interface, such as the phase field method and level set method. The second reason is the straightforward extension of the model to anisotropic simulations using experimentally derived interface properties. The third is that the data structure of the model is analogous to that of the experiment, allowing data to be easily transferred and the analysis of microstructural characteristics to be computed using the same codes for the experimental and simulated data. Furthermore, Nino and Johnson [30] showed that anisotropic threshold dynamics simulations produced triple junction geometries that were consistent with the Herring [59] condition.

There are different methods to incorporate the experimentally derived grain boundary energy into the evolution algorithm [60–64]. To consider a fully anisotropic TD method, we will follow [60], because it has no restriction on the choice of the grain boundary energy function that can be considered, and it is computationally less expensive than other available models as it only requires the GBE itself and not its derivatives. To evaluate the grain boundary energy, the five-parameter grain boundary function defined by Bulatov *et al*. (Bulatov-Reed-Kumar (BRK) energy function) is used [54]. Although this function is only an interpolation between 388 calculated GBE values from molecular dynamics simulation [65], it has been shown to be a good approximation of experimentally determined GBEs [66].

II. MATERIALS AND METHODS

A. Threshold dynamics

The threshold dynamics (TD) algorithm is a method to simulate free boundary motion by mean curvature and was initially introduced by Merriman, Bence, and Osher [57,58]. In this approach, each grain i is identified by a characteristic function $\mathbf{1}_{\Sigma_i^k}$, which has the value one within grain i and zero outside the grain. The set of position vectors within grain i at time t_k are denoted by Σ_i^k. To evolve a microstructure with N grains at time t_k and evaluate the microstructure at time $t_{k+1} > t_k$, Algorithm 1 [49,61] is used. In the convolution step, each grain's characteristic function is convolved with a kernel specific to each boundary, $K_{\delta t}^{i,j} = K_{\delta t}^{j,i}$. Typically, the kernels are defined such that they are maximum at the origin and decay to zero at infinity; the overall rate of the decay to zero depends on δt and the rate of the decay in each direction depends on the anisotropy of the grain boundary energy as described below [67]. At each point $\boldsymbol{x}$, the convolution operator computes the integral of the product between the characteristic function and the kernel, with the kernel repositioned so that its maximum is located at point $\boldsymbol{x}$. Hence, the value of the convolution ψ_i^k at point $\boldsymbol{x}$ deep inside grain i and far from the boundary remains zero while its value increases as $\boldsymbol{x}$ gets closer to the boundary and increases further outside of the grain. Note that the convolution value ψ_i^k highly depends on the curvature of the boundary as the convolution, which results from the overlap between the nonzero part of the kernel and the nonzero part of the characteristic function $\mathbf{1}_{\Sigma_j^k}$, can vary significantly depending on the shape of the grain. In the thresholding step, the characteristic function for each grain is redefined such that $\mathbf{1}_{\Sigma_i^{k+1}}$ at time t_{k+1} is equal to one at points where ψ_i is minimum compared to ψ_j for all other grains with $j = 1, ..., N$, and zero otherwise. This way, the boundaries are moved effectively by weighted mean curvature.

In the generalized form of the algorithm [49], $K_{\delta t}^{i,j}$ can be different for different grain boundaries. Under the assumption that the GBE for all boundaries is equal (isotropic GBE), the kernel $K_{\delta t}^{i,j} : \mathbb{R}^3 \to \mathbb{R}$ is the same for all grain boundaries and is equal to a Gaussian

$$K_{\delta t}^{i,j}(\boldsymbol{x}) = \frac{1}{(4\pi\,\delta t)^{3/2}} \exp\left(-\frac{|\boldsymbol{x}|^2}{4\delta t}\right), \tag{2.3}$$

which is spherically symmetric and decays with the same rate in all directions.

ALGORITHM 1. Anisotropic threshold dynamics.

Initialization: Given $\Sigma_1^k, ...\Sigma_N^k$ and time step size δt

Convolution:

$$\psi_i^k = \sum\nolimits_{\substack{j=1 \\ j\neq i}}^{N} K_{\delta t}^{i,j} * \mathbf{1}_{\Sigma_j^k} \tag{2.1}$$

Thresholding:

$$\Sigma_i^{k+1} = \left\{\boldsymbol{x} : \psi_i^k(\boldsymbol{x}) \leqslant \min_{j\neq i} \psi_j^k(\boldsymbol{x})\right\} \tag{2.2}$$

Extending this algorithm to cases where the GBE, σ, depends only on misorientation, $\Delta \boldsymbol{g}$ (three parameters model), is straightforward. In this case, all directions for the grain boundary normal are energetically equally favorable, hence a spherically symmetric kernel for the evolution of each interface can be used. To distinguish the difference between the energy of different grain boundaries caused by the misorientation, this spherically symmetric kernel can be scaled according to its energy and defines $K_{\delta t}^{i,j}$ for the boundary with adjacent grains i, j as [49]

$$K_{\delta t}^{i,j}(\boldsymbol{x}) = \frac{\sigma^{i,j}(\Delta \boldsymbol{g}^{i,j})}{(4\pi\,\delta t)^{3/2}} \exp\left(-\frac{|\boldsymbol{x}|^2}{4\delta t}\right). \tag{2.4}$$

The Read Shockley GBE [68] is an example of this case.

However, in the case that the GBE also depends on the inclination of the grain boundary, specific grain boundary normals are more favorable than others. Hence, a kernel that can capture this effect should not be spherically symmetric [67] which brings in more challenges compared to the previous case of the three-parameters model. Defining this kernel to result in the grain boundary velocity proportional to GBE has been the topic of several studies [60,61,63,64] and remains an active area of research.

In this study, we will use the kernel constructed by Bonnetier *et al.* [60] to simulate the anisotropic evolution of microstructure. The Fourier transformation of this kernel $\mathscr{F}\left[K_{\delta t}^{i,j}(\boldsymbol{x})\right]$ is

$$\hat{K}_{\delta t}^{i,j}(\boldsymbol{\xi}) = \mathscr{F}\left[K_{\delta t}^{i,j}(\boldsymbol{x})\right] = \frac{1}{\delta t^{3/2}} \exp\left(-(\tilde{\sigma}^{i,j}(\delta t\boldsymbol{\xi}))^2\right),$$
$$\tilde{\sigma}(\boldsymbol{x})^{i,j} = |\boldsymbol{x}|\sigma^{i,j}\left(\frac{\boldsymbol{x}}{|\boldsymbol{x}|}\right) \tag{2.5}$$

where $\sigma^{i,j} : \mathbb{S}^2 \to \mathbb{R}^+$ is the GBE function for all boundary inclinations for a given misorientation $\Delta \boldsymbol{g}^{i,j}$ between grain i, j, and $\tilde{\sigma}^{i,j}$ is an extension of $\sigma^{i,j}$ such that $\tilde{\sigma}^{i,j} : \mathbb{R}^3 \to \mathbb{R}^+$. Note that for evaluating the convolution step (2.1), in the computational setting we use $f * g = \mathscr{F}^{-1}[\mathscr{F}[f]\mathscr{F}[g]]$, so there is no need for computing this kernel in the physical domain [69]. Furthermore, in the kernel used here, the mobility of the interface is embedded such that it is equal to the GBE. There are recent attempts to derive more general kernels where mobility and GBE can be assigned independently, and this is still an active area of the research [63].

According to Algorithm 1, using an anisotropic kernel will only affect the convolved value ψ_i^k, which is the input to the thresholding step. The convolved value ψ_i^k is the result of the convolution between the anisotropic kernel and the characteristic function $\mathbf{1}_{\Sigma_j^k}$. Hence, a simplified extension of the Algorithm 1 to the five-parameter anisotropic GBE can be also achieved by changing the characteristic function $\mathbf{1}_{\Sigma_j^k}$ according to the GBE and keeping the kernel spherically symmetric Gaussian. Nino and Johnson [30] achieved this by replacing $\mathbf{1}_{\Sigma_j^k}$ with $\sigma^{i,j}(\boldsymbol{n})\mathbf{1}_{\Sigma_j^k}$. Although methods based on defining an anisotropic kernel following the grain boundary energy and mobility anisotropy are derived from energy minimization [63], more study is required to understand if the simplified version of Nino and Johnson [30] is indeed equivalent to a weighted mean curvature flow and minimizes the energy.

B. Grain boundary energy

Experiments show that the grain boundary energy is a function of five macroscopic parameters, i.e., lattice misorientation between the two adjacent grains (three degrees of freedom), and the inclination of the grain boundary plane (two degrees of freedom) [47]. There are different methods for the representation of these five parameters. The most common way is to represent the misorientation between the adjacent grains and plane boundary inclinations separately. For example, from experimental measurements considered in this study, for each grain, the rotation of the lattice of each grain relative to a fixed sample frame coordinate system is measured and is represented through a set of Euler angles (ϕ_1, Φ, ϕ_2) for rotation around the (Z, X, Z) axes. Once the Euler angles are given, the rotation matrix $\boldsymbol{g}_i$ for rotating the sample frame to the frame of grain i can be computed, and $\Delta \boldsymbol{g} = \boldsymbol{g}_i \boldsymbol{g}_j^T$ will give the transformation of the lattice of grain j to the lattice of grain i, which is a representation of misorientation between grains i and j. Independent of misorientation measurements and calculations, the inclination of each point in the grain boundary plane $\boldsymbol{n}$ is computed after the reconstruction and triangulation of grain boundaries in DREAM.3D software [70]. Hence, a full five-parameter representation of the grain boundary is given through a normal vector $\boldsymbol{n}$ and a transformation matrix $\Delta \boldsymbol{g}$.

In this study, we use the BRK energy function to evaluate the GBE for any given five parameters for a grain boundary in Ni. The BRK GBE function is a nonlinear interpolation based on 388 different measured grain boundary energies, provided through a MATLAB function as Supplementary Data in [54]. This function is a piecewise interpolation that extends from each cusp in the energy landscape and is consistent with the symmetry of the material.

Despite the mentioned representation from the experimental data where grain boundary misorientation and plane boundary inclination are represented separately, the input of BRK GBE model is two three-by-three matrices labeled $\boldsymbol{P}$ and $\boldsymbol{Q}$ in which both grain boundary misorientation and plane boundary inclination are combined and represented through these two rotation matrices. A detailed procedure for converting Euler angles and normal vector to the $\boldsymbol{PQ}$ representation is presented in Appendix.

C. Model validation

In this section, we validate that the choice of the anisotropic kernel can realistically capture the grain evolution. We grow a spherical grain located in its melt using different interface energy functions of the form (2.6) by using kernel (2.5). The result of our simulation is compared with the result of the front tracking simulations computed by Mohles [71]. Following [71], we consider different energy functions of the following form:

$$GBE = 1 + \alpha(|n_x|^m + |n_y|^m + |n_z|^m) \tag{2.6}$$

where n_x, n_y, n_z are different components of boundary plane normal. The equilibrium shape of the grain, which is expected to be the Wulff shape of the energy function, is shown in Fig. 1 and matches the equilibrium shape simulated using the front tracking method (Fig. 7 in [71]) for two sets of parameters

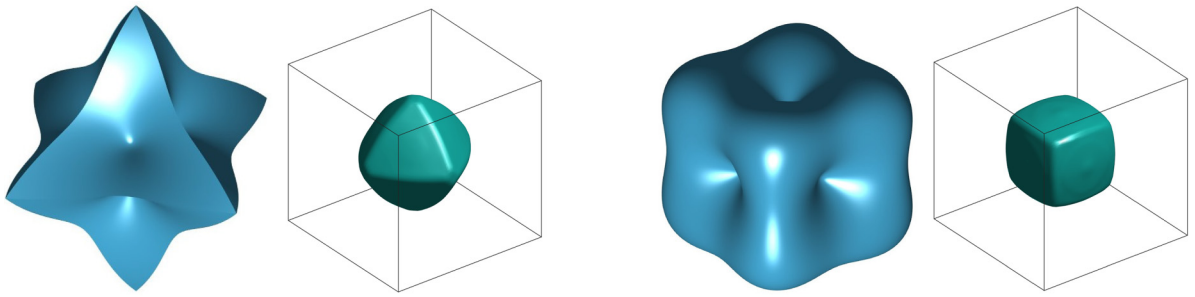

(a) $m = 1$, $\alpha = -0.5$ (b) $m = 4$, $\alpha = -0.7$

FIG. 1. Simulated equilibrium shape (right) of an initially spherical grain in its melt in a box of size 64^3 (outlined by black lines) using different surface energy (left) of the form (2.6).

$m = 1, \alpha = -0.5$, and $m = 4, \alpha = -0.7$. As expected, the inclination of the facets of the equilibrated grains aligns with the direction of minimum energy ([1 1 1] for the GBE in Fig. 1(a), and [1 0 0] for the GBE in Fig. 1(b)). Thus, the choice of the anisotropic kernel can capture the expected behavior during grain growth.

Furthermore, a sensitive test of the anisotropic simulation is to observe the evolution of the GB plane distribution, as the GB energy anisotropy influences this [72]. Given that the Σ3 GB of Ni has the minimum energy at the [111] twin position, an increase in its relative area is both expected and observed in the simulation. Figure 2 shows the continuous increase in the relative area of twin boundaries for different timesteps of a simulation, starting from An4 with a relative area of twin boundaries of 547 multiples of a random distribution (MRD) and the ending when the average grain size of An5 is reached, using the BRK energy function (An4 and An5 refer to experimental states defined in Sec. III).

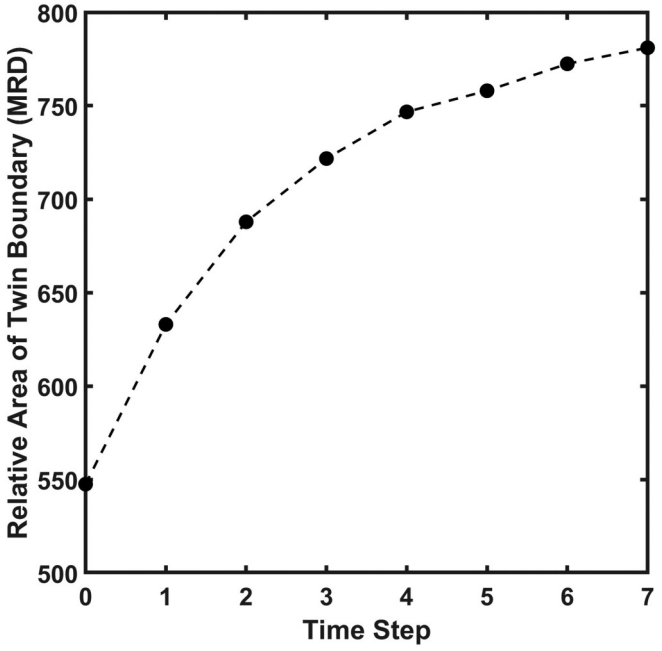

FIG. 2. Relative area of twin boundary (MRD) for different timesteps of a simulation started from An4 with the intensity of 547 and the end point of reaching the average grain size of An5.

D. Computational challenges of anisotropic simulation

One main difference between the isotropic and anisotropic simulation is that in the isotropic simulation the kernel is the same for all grain pairs, and hence it can be computed once at the start of the simulation and used at any time later during the simulation. However, in the full anisotropic simulation, the convolution kernel is different for each grain pair and there is no linear relation between kernels, as in the case of GBE only being a function of misorientation. Hence, a key challenge is that the experimental volume contains a large number of different GB types with an approximate number of distinct grain boundaries of 34000 in each microstructure. Additionally, to evaluate the nonspherically symmetric anisotropic kernel (2.5) for each two-grain pair with a given grain boundary misorientation, the GBE for all inclinations of the boundary plane is required.

While the energies are potentially available from the BRK function, evaluating them for all points in a kernel is prohibitively expensive numerically. Therefore, we define a coarser grid including 6192 different normal vectors uniformly distributed on a sphere. For each grain boundary misorientation, we store the energy at these 6192 different inclinations, at the start of the simulation. We then use the nearest interpolation method to compute energy values on the finer grid of the simulation.

E. Experimental data and simulations

This paper aims to compare the experimentally observed microstructure evolution of a high-purity Ni sample during annealing with simulated microstructures using both isotropic and anisotropic grain boundary energy. The sample was measured at six different times using nearfield high energy x-ray diffraction microscopy [56,73]. The sample underwent annealing for about 30 minutes at 800°C between each measurement. Previous studies have outlined the specifics of data acquisition and interpretation [56,74,75]. Six repeated measurements of the same sample volume were used to reconstruct the shapes and orientations of grains after successive annealing treatments [74,75]. The data are represented as a set of discrete voxels using DREAM.3D [55,70] and are referred to as An0, An1, An2, An3, An4, and An5 throughout the paper. The microstructures contained 2400 to 3000 grains made up of voxels with dimensions of $2.3 \times 2.3 \times 4.0\,\mu m^3$. In the initial state, there was an average of 2347 voxels per

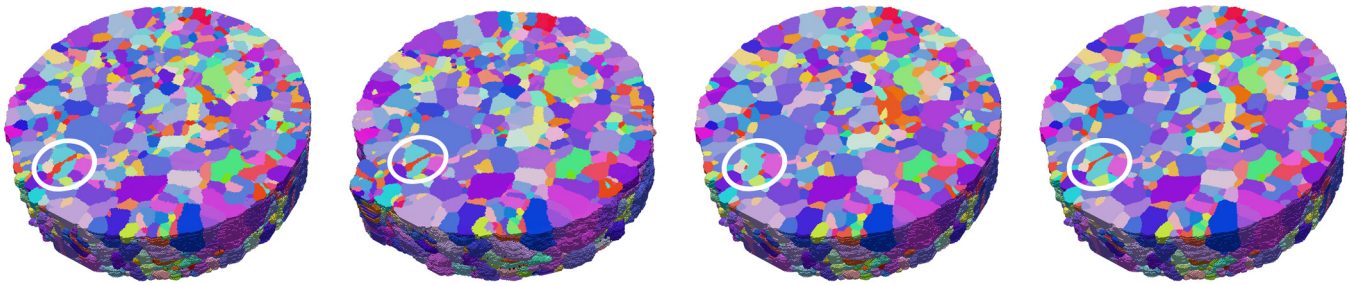

(a) Initial state (An0) (b) Experiment (An1) (c) Isotropic simulation (d) Anisotropic simulation

FIG. 3. Experimentally measured and simulated microstructures. In each case, the diameter of the cylinder is about 1 mm.

grain. We note that the data used here is the same that was used in our previous isotropic simulation [31], with one important difference. In the previous study, all twinned grains were merged to form single grains, in an effort to ameliorate the known anisotropy of the energy. In contrast, all twins were preserved in the present study.

The first five reconstructed microstructures (An0 to An4) were considered as an initial state of different simulations independently. Both isotropic and anisotropic simulation was performed for each of the five initial states. The average grain size increases throughout the simulation and experimental annealing, and the simulations were terminated when the average grain size reaches the average grain size in the next experimental anneal step [31]. All grain boundary properties (relative area, curvature, velocity) were calculated using methods described in previous publications [42,44] and summarized below.

F. Grain boundary properties

The analysis of the experimental data and simulations involved calculation of the grain boundary relative areas, curvatures, and velocities. The calculations begin by converting the voxelated grain boundaries to meshed interfaces in DREAM.3D [70]. The relative areas of specific boundaries were determined using the method of Glowinski and Morawiec [76]. The grain boundary curvature was calculated as the area weighted mean curvature of all of the mesh elements belonging to a certain boundary, using DREAM.3D [44,77]. The migration velocity of each boundary was determined based on the volume of voxels exchanged across the boundary; detailed information can be found in previous publications [42,44].

III. RESULTS

The cylindrical Ni sample in the initial experimental state (An0), and An1 are depicted in Figs. 3(a) and 3(b), where the 2972 and 2669 grains are colored by orientation. Figures 3(c) and 3(d) show the evolved microstructure from An0 to An1 using isotropic and anisotropic simulations, respectively. A cursory comparison shows only small differences between the four microstructures. However, one exemplary feature is highlighted by the white oval. A twin (red) bisects a blue colored grain. In the experiment and in the anisotropic simulation, the twin is preserved. However, in the isotropic simulation, it is eliminated. This is because when all grain boundary energies are the same, spheroidal, energy minimizing grain shapes are preferred over grains with high aspect ratios. In the remainder of this section, we use distributions of properties to compare the microstructure more systematically.

The behavior of the evolved microstructure during the experiment, isotropic, and anisotropic simulations from different perspectives is compared. Since the simulations were performed independently for different anneal stages as the initial state of the simulation, the result of each simulation is only compared with the next experimental anneal step. The following notation is considered to present the results in this section:

(1) An0–1: The experiment/simulation started with the An0 microstructure and terminated when the average grain size was equal to the average grain size of the An1 experiment.

(2) Initial state: Experimental data of An0.

(3) Experiment: Microstructure evolved experimentally and stopped at An1.

(4) Anisotropic simulation: The output of the simulation using an anisotropic kernel in Algorithm 1. The input is An0 experimental data and the simulation was stopped when the average grain size reached the average grain size of An1.

(5) Isotropic simulation: The output of the simulation using an isotropic kernel in Algorithm 1. The input is An0 experimental data and the simulation was stopped when the average grain size reached the average grain size of An1.

A similar notation is used for An1-2, An2-3, An3-4, and An4-5.

Two main statistical features that are expected to be captured in the anisotropic simulation are the energy distribution of grain boundaries and the relative area of Σ3 twin boundaries. Figures 4 and 5 show the relative area of the twin boundaries for simulated and experimental anneal steps and the microstructure energy per unit area of the grain boundaries. For each step, compared to the initial state, the relative area of the twin boundaries increases in both the experiment and anisotropic simulations, while it always decreases in the isotropic simulation. Similarly, compared to the initial state, the energy per unit area decreases (except for An3-4) and the anisotropic simulation always decreases the energy. The small increase in energy for An3-4 might be the result of uncertainties in the experiment and reconstruction. Note that since the uniform grain boundary energy of one is assigned to all the boundaries in isotropic simulation, the energy per unit area always remains one and is not relevant for the comparison. The increase in the relative area of the twin boundary

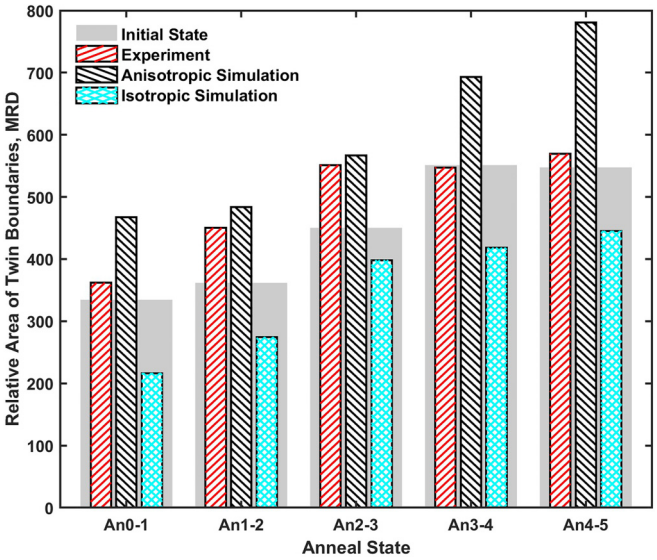

FIG. 4. The twin boundary relative area for experimental and simulated data at different anneal states.

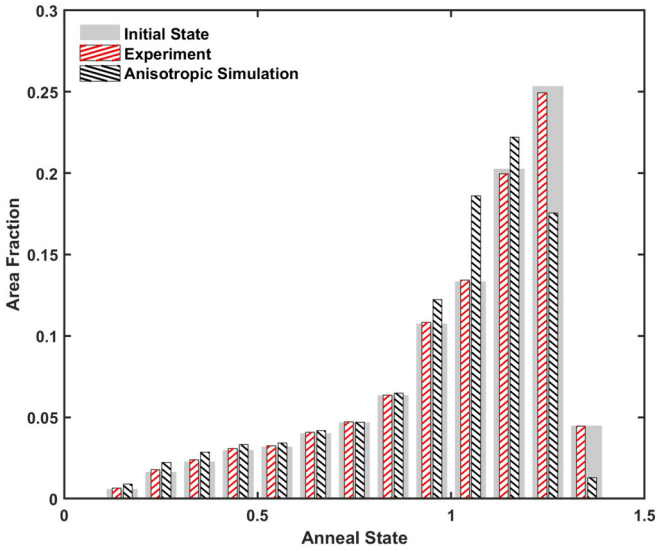

FIG. 6. Distribution of simulated and experimental GBEs combined for all anneal states.

and the decrease in the average grain boundary energy in the anisotropic simulation is always greater than in the experiment; this will be discussed later in Sec. IV.

Figure 6 looks more closely at the energy distribution of the simulated and experimental data for all anneal stages combined together. The thick gray bars behind the thinner bars show the energy distribution for the initial state of the experiment and simulation, and the two thinner bars show the GBE distribution for the anisotropic and next experimental anneal state. For the lower-energy grain boundaries, there are more boundaries in the final states of the experiment and simulation and for the higher-energy boundaries, there are fewer. A comparison of these distributions shows that the experiment and anisotropic simulation shift the distributions so that there are more boundaries with lower energy.

Two sources of differences between the simulated and observed microstructures are differences in the volume changes of grains and differences in the neighborhoods. In [31], it was shown that these effects are correlated. To examine whether or not this occurs in the current simulation, we compare the volume prediction error (VPE) with the topological error (TE) for individual grains. VPE and TE are defined as follows:

$$\Delta N_s = N_{\text{sim}} - N_{\text{exp(initial)}}, \tag{3.1}$$

$$\Delta N_e = N_{\text{exp(final)}} - N_{\text{exp(initial)}}, \tag{3.2}$$

$$TE = \Delta N_s - \Delta N_e \tag{3.3}$$

$$VPE = \frac{V_s - V_e}{V_e} \tag{3.4}$$

where $N_{\text{exp(initial)}}$ is the number of neighbors of grain in the initial experiment state, $N_{\text{exp(final)}}$ is the number of neighbors of the same grain in the final experiment state, and N_{sim} is the number of neighbors of the same grain in the final simulation state. VPE is the fractional difference in volume predicted by the simulation of the final anneal state (V_s) and experimental final state (V_e). TE is the difference in ΔN for each grain between simulation and experiment. In other words, TE is the error in predicting topological evolution by the simulation. Figure 7 plots the volume prediction error as a function of topological error for isotropic and anisotropic simulations. A low VPE indicates a small difference between the final volume predicted and the actual final volume of the grain. A high-TE value means there is a large error in predicting the topological evolution of the grains. Similar behavior of isotropic and anisotropic simulation in VPE vs TE suggests that considering energy anisotropy does not improve this aspect of the simulation.

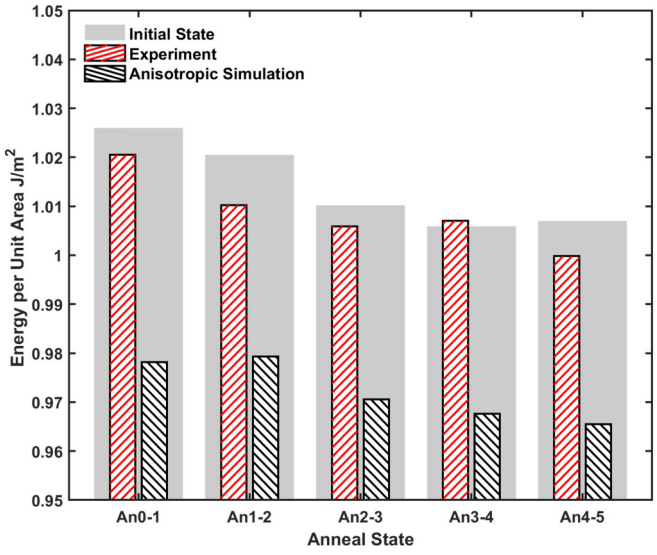

FIG. 5. Energy per unit area for experimental and simulated data at different anneal states.

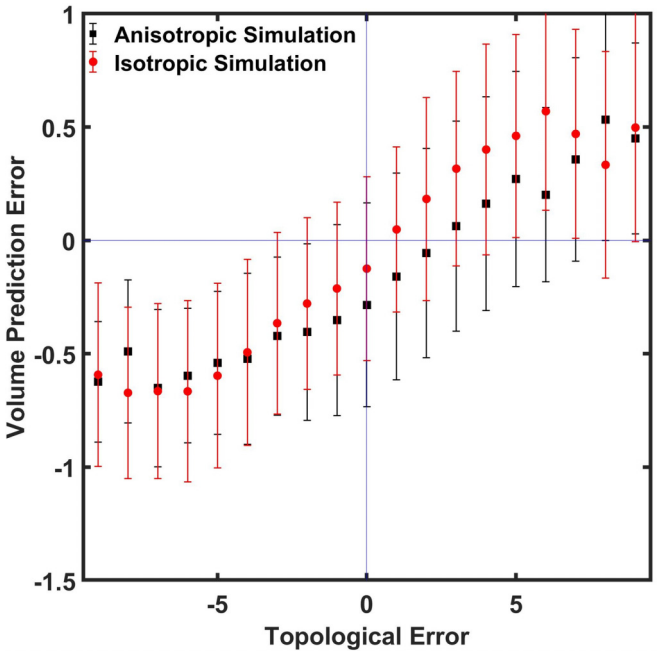

FIG. 7. The volume prediction error (VPE) as a function of topological error (TE). VPE is the fractional difference in predicted and observed grain volume. TE is the difference in grain face evolution between simulation and experiment.

Measurements of the grain boundary velocity and curvature from the experimental data showed no correlation between these quantities [42]. This unexpected result was also reported for α-Fe [44] and $SrTiO_3$ [43]. As illustrated in Fig. 8, the simulated data also lacks a correlation between curvature and velocity, consistent with the experiment. When interpreting this result, it is important to note that the curvature data is always from the initial (experimental) data, so is independent of the simulation. Similarly, the velocity calculation also incorporates information from the initial state, so this undoubtedly influences the result. It is somewhat surprising that the isotropic simulation does not show a correlation between velocity and curvature. When the same method was used to simulate the evolution of α-Fe with isotropic grain boundary energies, a strong correlation between velocity and curvature was found [44]. The one difference is that the grain shapes in the α-Fe were equiaxed, while the Ni microstructure contains many nonequiaxed shapes that result from twinning. Instantiating the simulation with this structure "imprints" this anisotropy in the microstructure and this is apparently enough to disrupt any correlation between velocity and curvature that the simulation might otherwise produce. Therefore, the absence of a correlation between curvature and velocity in the anisotropic simulation cannot solely be attributed to the grain boundary energy anisotropy.

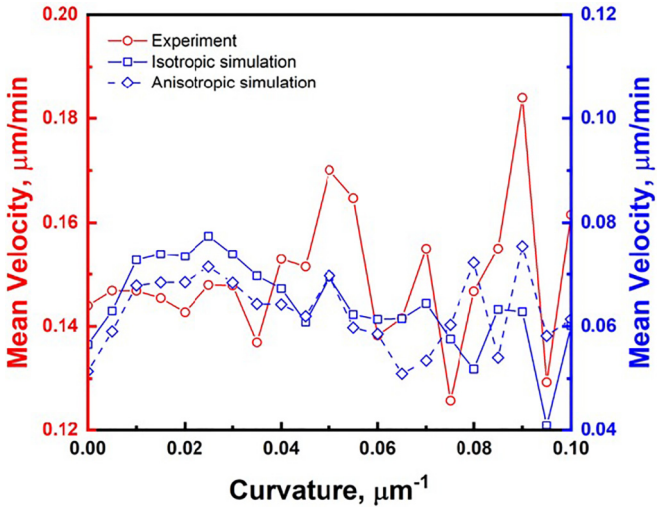

FIG. 8. Mean velocity as a function of curvature in experiment and simulations.

IV. DISCUSSION

The results of the simulations reproduce the decrease in the average energy of grain boundaries through grain boundary replacement [45], a key phenomenon found in the experiment. The simulations show that the decrease in the average energy is associated with a decrease in the fraction of high-energy grain boundaries and an increase in the fraction of low-energy grain boundaries. A key finding of this paper- is that this phenomenon emerged simply by introducing an anisotropic energy distribution. In other words, there was no need to introduce a new physical mechanism in the model. The simulation is constructed to reduce the total area. The results suggest that when multiple possible grain boundary migration paths are possible, on average, the one that is selected is the one that reduces the area in such a way that lower-energy grain boundaries are increased in area at the expense of higher-energy boundaries. This process leads to the results in Figs. 5 and 6. The accumulation of low-energy grain boundaries during grain growth has been observed in experiment [47] and in simulations [30,38,53] before, but this work goes further to provide a direct comparison between experiment and simulation showing that observed features of the microstructure emerge by assuming realistic anisotropic energies.

One important difference between the experiment and the simulation is that the grain boundary replacement process is more significant in the simulation. For example, the decrease in the average energy at each time step in the experiment is $< 1\%$ while in the simulation it was of the order of 4% (see Fig. 5). The most likely source of this difference is the difference between the energy anisotropy in the simulation and experiment. The simulation used the BRK energies at 0 K [54], while the experiment [56] was carried out at 1073 K. The differences in the energies among boundaries is certainly smaller at 1073 K, and this is expected to decrease the driving force for the grain boundary replacement process. Simulations conducted with scaled energies showed that decreasing the energy differences slowed the decrease in the average energy, with the isotropic case presented here being the extreme

example. However, scaling the energies in a realistic way proved challenging. The assignment of temperature-dependent grain boundary properties would make it possible to simulate the effect of temperature on microstructure evolution.

When comparing the results of the simulation and experiment, one should keep in mind that the simulation is instantiated with experimental data, seeding the process with the ground truth at that time step. Such a simulation is obviously better situated to reproduce the experiment than starting from a nonphysical state. While one might guess that this guarantees the simulation produces a realistic microstructure, the results show otherwise. As illustrated in Fig. 4, the simulation with isotropic grain boundary energies evolves the microstructure in the wrong direction; the relative areas of twin boundaries decreases with time while the experiment and anisotropic simulation both increase the relative areas of the twins. In other words, even though the simulation is provided with the correct starting point, it evolves in the wrong direction. The option of instantiating the simulation with a starting point different from the observed microstructure could also be informative, but this seems less likely to lead to a better understanding of the physical process that occurs in real grain growth.

Grain-by-grain comparisons of microstructure evolution have been unsuccessful in the past [27,55,78] and the implementation of anisotropic energies has not improved the situation, as illustrated in Fig. 7. The basic problem is that as soon as a single critical event (the disappearance of a grain face for example) is predicted incorrectly, the microstructure evolves along a different path. The energy distribution used in the simulation is thought to be a reasonable approximation of the energies at 0 K, but this approximation deviates from the true energy distribution at the experimental temperature, and this might contribute to differences in the evolutions. Even if the energy was completely accurate, there is evidence that some aspects of grain boundary migration are not entirely reproducible in atomistic simulations [79]. In other words, when grain boundary migration is simulated many times by molecular dynamics, the outcome is not fully reproducible. If so, there is no possibility of reproducing the exact sequence of critical events in microstructure evolution, even if the physical process in the experiment is fully deterministic.

The observed reduction in grain boundary energy provides an additional energy dissipation mechanism during grain growth, as described previously [45]. This is an additional driving force that influences grain boundary migration and is absent in simulations with isotropic grain boundary energies. Previous reports that the grain boundary character distribution evolves in response to assumed anisotropic energies [30,38,51,53] and the results presented here that the assumption of realistic energies leads to simulated results that reproduce many features of the experiment indicate that anisotropic grain boundary energies are required input for realistic simulations. While this seems to add a complexity to the simulations, realistic, five-parameter, grain boundary energy functions for the fcc [54] and bcc [80] structures are available and, at least for the TD simulation, it is not necessary to alter the energy minimizing procedure.

V. CONCLUSIONS

We have compared the experimentally observed microstructure evolution of a Ni sample with isotropic and anisotropic simulations. In the anisotropic simulation, the grain boundary energies were defined by the BRK energy function. The assumption of anisotropic grain boundary energies leads to an increase in the relative areas of low-energy twin boundaries and a change in the grain boundary energy distribution that reduces the average grain boundary energy. These changes result from the anisotropic grain boundary energy, without any changes in the energy minimizing algorithm, and do not occur when isotropic energies are assumed. The results indicate that realistic simulations of grain growth in polycrystals require anisotropic grain boundary energies that approximate those in the real material.

A version of the code developed for this study is available at Github [81]. And, the data used for this paper are available online [82].

ACKNOWLEDGMENTS

This work was supported by the National Science Foundation under DMREF Grant No. 2118945. We acknowledge NSF for XSEDE computing resources provided by Pittsburgh Supercomputing Center. S.K.N. was partially supported by the Bushnell Fellowship and the MIT Postdoctoral Fellowship Program for Engineering Excellence (PFPFEE). This research used resources of the Advanced Photon Source, a U.S. Department of Energy (DOE) Office of Science User Facility operated for the DOE Office of Science by Argonne National Laboratory under Contract No. DE-AC02-06CH11357.

APPENDIX: EULER ANGLES AND NORMAL VECTOR TO *PQ* REPRESENTATION

Matrices $\boldsymbol{P}$ and $\boldsymbol{Q}$ are rotation matrices from the frame of grain i and j to a reference frame where the normal of the boundary plane is aligned with the x axis, respectively. Hence,

(1) the first rows of $\boldsymbol{P}$ and $\boldsymbol{Q}$ represent the normal boundary plane in the frame aligned with the lattice of grain i, and the lattice of grain j, respectively;

(2) the rotation matrix from the lattice of grain j to the lattice of grain i, i.e., $\Delta \boldsymbol{g} = \boldsymbol{g}_i \boldsymbol{g}_j^T$, is equal to $\boldsymbol{P}^T \boldsymbol{Q}$.

Given a boundary plane normal $\boldsymbol{n}$ represented in the sample frame from triangulation, the first row of $\boldsymbol{P}$ is $\boldsymbol{g}_1 \boldsymbol{n}$. Since $\boldsymbol{P}$ is a rotation matrix, all its rows should be perpendicular to each other, hence the second row of $\boldsymbol{P}$ can be any normalized vector perpendicular to the first row. The third row is perpendicular to rows 1 and 2, i.e., the cross product of row 1 and row 2. Finally, $\boldsymbol{Q}$ can be computed using the equality of $\Delta \boldsymbol{g} = \boldsymbol{P}^T \boldsymbol{Q}$. Note that the second row of matrix $\boldsymbol{P}$ is not unique, hence $\boldsymbol{P}$ and $\boldsymbol{Q}$ are not unique, but any $\boldsymbol{P}$ and $\boldsymbol{Q}$ that satisfies conditions 1 and 2 will result in the same energy value.

[1] F. D. Fischer, J. Svoboda, E. Gamsjäger, and E. R. Oberaigner, From distribution functions to evolution equations for grain growth and coarsening, Acta Mater. **56**, 5395 (2008).

[2] G. Gottstein, D. A. Molodov, and L. S. Shvindlerman, Grain boundary migration in metals: Recent developments, Interface Sci. **6**, 7 (1998).

[3] M. Hillert, On the theory of normal and abnormal grain growth, Acta Metall. **13**, 227 (1965).

[4] G. B. Bizana and L. A. Barrales-Mora, Kinetics of grain boundary migration in nanosized Al polycrystals, Acta Mater. **260**, 119261 (2023).

[5] D. Chen and Y. Kulkarni, Atomistic modeling of grain boundary motion as a random walk, Phys. Rev. Mater. **2**, 093605 (2018).

[6] D. Chen, S. Xu, and Y. Kulkarni, Atomistic mechanism for vacancy-enhanced grain boundary migration, Phys. Rev. Mater. **4**, 033602 (2020).

[7] E. A. Holm and S. M. Foiles, How grain growth stops: A mechanism for grain-growth stagnation in pure materials, Science **328**, 1138 (2010).

[8] R.-J. Jhan and P. D. Bristowe, A molecular dynamics study of grain boundary migration without the participation of secondary grain boundary dislocations, Scr. Metall. Mater. **24**, 1313 (1990).

[9] C. P. Race, J. von Pezold, and J. Neugebauer, Role of the mesoscale in migration kinetics of flat grain boundaries, Phys. Rev. B **89**, 214110 (2014).

[10] M. Upmanyu, D. J. Srolovitz, L. S. Shvindlerman, and G. Gottstein, Triple junction mobility: A molecular dynamics study, Interface Sci. **7**, 307 (1999).

[11] H. Zhang, D. J. Srolovitz, J. F. Douglas, and J. A. Warren, Characterization of atomic motion governing grain boundary migration, Phys. Rev. B **74**, 115404 (2006).

[12] M. P. Anderson, G. S. Grest, and D. J. Srolovitz, Computer simulation of normal grain growth in three dimensions, Philos. Mag. B **59**, 293 (1989).

[13] D. J. Srolovitz, M. P. Anderson, P. S. Sahni, and G. S. Grest, Computer simulation of grain growth—II. Grain size distribution, topology, and local dynamics, Acta Metall. **32**, 793 (1984).

[14] D. J. Srolovitz, Grain growth phenomena in films: A Monte Carlo approach, J. Vac. Sci. Technol. A **4**, 2925 (1986).

[15] N. C. Admal, J. Segurado, and J. Marian, A three-dimensional misorientation axis-and inclination-dependent Kobayashi–Warren–Carter grain boundary model, J. Mech. Phys. Solids **128**, 32 (2019).

[16] A. Adland, Y. Xu, and A. Karma, Unified theoretical framework for polycrystalline pattern evolution, Phys. Rev. Lett. **110**, 265504 (2013).

[17] M. Bjerre, J. M. Tarp, L. Angheluta, and J. Mathiesen, Rotation-induced grain growth and stagnation in phase-field crystal models, Phys. Rev. E **88**, 020401(R) (2013).

[18] L.-Q. Chen, Phase-field models for microstructure evolution, Annu. Rev. Mater. Res. **32**, 113 (2002).

[19] S.-I. Ito, H. Nagao, T. Kurokawa, T. Kasuya, and J. Inoue, Bayesian inference of grain growth prediction via multi-phase-field models, Phys. Rev. Mater. **3**, 053404 (2019).

[20] C. E. Krill III and L.-Q. Chen, Computer simulation of 3-D grain growth using a phase-field model, Acta Mater. **50**, 3059 (2002).

[21] B. Korbuly, T. Pusztai, H. Henry, M. Plapp, M. Apel, and L. Gránásy, Grain coarsening in two-dimensional phase-field models with an orientation field, Phys. Rev. E **95**, 053303 (2017).

[22] R. D. Kamachali and I. Steinbach, 3-D phase-field simulation of grain growth: Topological analysis versus mean-field approximations, Acta Mater. **60**, 2719 (2012).

[23] R. Kobayashi, J. A. Warren, and W. C. Carter, Vector-valued phase field model for crystallization and grain boundary formation, Physica D **119**, 415 (1998).

[24] A. Kazaryan, Y. Wang, S. A. Dregia, and B. R. Patton, Grain growth in systems with anisotropic boundary mobility: Analytical model and computer simulation, Phys. Rev. B **63**, 184102 (2001).

[25] N. Moelans, B. Blanpain, and P. Wollants, Quantitative analysis of grain boundary properties in a generalized phase field model for grain growth in anisotropic systems, Phys. Rev. B **78**, 024113 (2008).

[26] N. Moelans, New phase-field model for polycrystalline systems with anisotropic grain boundary properties, Mater. Design **217**, 110592 (2022).

[27] I. M. McKenna, S. O. Poulsen, E. M. Lauridsen, W. Ludwig, and P. W. Voorhees, Grain growth in four dimensions: A comparison between simulation and experiment, Acta Mater. **78**, 125 (2014).

[28] M. Tang, W. C. Carter, and R. M. Cannon, Diffuse interface model for structural transitions of grain boundaries, Phys. Rev. B **73**, 024102 (2006).

[29] L. Vanherpe, N. Moelans, B. Blanpain, and S. Vandewalle, Bounding box algorithm for three-dimensional phase-field simulations of microstructural evolution in polycrystalline materials, Phys. Rev. E **76**, 056702 (2007).

[30] J. D. Niño and O. K. Johnson, Influence of grain boundary energy anisotropy on the evolution of grain boundary network structure during 3D anisotropic grain growth, Comput. Mater. Sci. **217**, 111879 (2023).

[31] X. Peng, A. Bhattacharya, S. K. Naghibzadeh, D. Kinderlehrer, R. Suter, K. Dayal, and G. S. Rohrer, Comparison of simulated and measured grain volume changes during grain growth, Phys. Rev. Mater. **6**, 033402 (2022).

[32] P. Bardsley, K. Barmak, E. Eggeling, Y. Epshteyn, D. Kinderlehrer, and S. Ta'asan, Towards a gradient flow for microstructure, Rend. Lincei Mat. Appl. **28**, 777 (2017).

[33] K. Barmak, E. Eggeling, M. Emelianenko, Y. Epshteyn, D. Kinderlehrer, R. Sharp, and S. Ta'asan, Critical events, entropy, and the grain boundary character distribution, Phys. Rev. B **83**, 134117 (2011).

[34] W. L. Bragg and J. F. Nye, A dynamical model of a crystal structure, Proc. R. Soc. London A **190**, 474 (1947).

[35] D. Chen, T. Ghoneim, and Y. Kulkarni, Effect of pinning particles on grain boundary motion from interface random walk, Appl. Phys. Lett. **111**, 161606 (2017).

[36] S. Florez, K. Alvarado, B. Murgas, N. Bozzolo, D. Chatain, C. E. Krill III, M. Wang, G. S. Rohrer, and M. Bernacki, Statistical behaviour of interfaces subjected to curvature flow and torque effects applied to microstructural evolutions, Acta Mater. **222**, 117459 (2022).

[37] J. Farjas and P. Roura, Numerical model of solid phase transformations governed by nucleation and growth: Microstructure development during isothermal crystallization, Phys. Rev. B **75**, 184112 (2007).

[38] J. Gruber, D. C. George, A. P. Kuprat, G. S. Rohrer, and A. D. Rollett, Effect of anisotropic grain boundary properties on grain boundary plane distributions during grain growth, Scr. Mater. **53**, 351 (2005).

[39] F. J. Humphreys, Modelling microstructural evolution during annealing, Modell. Simul. Mater. Sci. Eng. **8**, 893 (2000).

[40] W. W. Mullins and J. Vinals, Scaling in linear bubble models of grain growth, Acta Metall. Mater. **41**, 1359 (1993).

[41] D. Moldovan, V. Yamakov, D. Wolf, and S. R. Phillpot, Scaling behavior of grain-rotation-induced grain growth, Phys. Rev. Lett. **89**, 206101 (2002).

[42] A. Bhattacharya, Y.-F. Shen, C. M. Hefferan, S. F. Li, J. Lind, R. M. Suter, C. E. Krill III, and G. S. Rohrer, Grain boundary velocity and curvature are not correlated in Ni polycrystals, Science **374**, 189 (2021).

[43] V. Muralikrishnan, H. Liu, L. Yang, B. Conry, C. J. Marvel, M. P. Harmer, G. S. Rohrer, M. R. Tonks, R. M. Suter, C. E. Krill III, Observations of unexpected grain boundary migration in $SrTiO_3$, Scr. Mater. **222**, 115055 (2023).

[44] Z. Xu, Y.-F. Shen, S. K. Naghibzadeh, X. Peng, V. Muralikrishnan, S. Maddali, D. Menasche, A. R. Krause, K. Dayal, R. M. Suter, Grain boundary migration in polycrystalline α-Fe, Acta Mater. **264**, 119541 (2024).

[45] Z. Xu, C. M. Hefferan, S. F. Li, J. Lind, R. M. Suter, F. Abdeljawad, and G. S. Rohrer, Energy dissipation by grain boundary replacement during grain growth, Scr. Mater. **230**, 115405 (2023).

[46] S. Ratanaphan, D. L. Olmsted, V. V. Bulatov, E. A. Holm, A. D. Rollett, and G. S. Rohrer, Grain boundary energies in body-centered cubic metals, Acta Mater. **88**, 346 (2015).

[47] G. S. Rohrer, Grain boundary energy anisotropy: a review, J. Mater. Sci. **46**, 5881 (2011).

[48] M. Elsey, S. Esedoḡlu, P. Smereka, Simulations of anisotropic grain growth: Efficient algorithms and misorientation distributions, Acta Mater. **61**, 2033 (2013).

[49] S. Esedoḡ Lu and F. Otto, Threshold dynamics for networks with arbitrary surface tensions, Commun. Pure Appl. Math. **68**, 808 (2015).

[50] H. Hallberg, Influence of anisotropic grain boundary properties on the evolution of grain boundary character distribution during grain growth—A 2D level set study, Modell. Simul. Mater. Sci. Eng. **22**, 085005 (2014).

[51] H. Salama, J. Kundin, O. Shchyglo, V. Mohles, K. Marquardt, and I. Steinbach, Role of inclination dependence of grain boundary energy on the microstructure evolution during grain growth, Acta Mater. **188**, 641 (2020).

[52] H. Hallberg and V. V. Bulatov, Modeling of grain growth under fully anisotropic grain boundary energy, Modell. Simul. Mater. Sci. Eng. **27**, 045002 (2019).

[53] H.-K. Kim, S. G. Kim, W. Dong, I. Steinbach, and B.-J. Lee, Phase-field modeling for 3D grain growth based on a grain boundary energy database, Modell. Simul. Mater. Sci. Eng. **22**, 034004 (2014).

[54] V. V. Bulatov, B. W. Reed, and M. Kumar, Grain boundary energy function for fcc metals, Acta Mater. **65**, 161 (2014).

[55] A. Bhattacharya, Y.-F. Shen, C. M. Hefferan, S. F. Li, J. Lind, R. M. Suter, and G. S. Rohrer, Three-dimensional observations of grain volume changes during annealing of polycrystalline Ni, Acta Mater. **167**, 40 (2019).

[56] C. M. Hefferan, S. F. Li, J. Lind, U. Lienert, A. D. Rollett, P. Wynblatt, and R. M. Suter, Statistics of high purity nickel microstructure from high energy x-ray diffraction microscopy, Comput. Mater. Cont. **14**, 209 (2009).

[57] B. Merriman, J. K. Bence, and S. Osher, Diffusion generated motion by mean curvature, CAM Report 92-18, Department of Mathematics, University of California, Los Angeles, 1992.

[58] B. Merriman, J. K. Bence, and S. J. Osher, Motion of multiple junctions: A level set approach, J. Comput. Phys. **112**, 334 (1994).

[59] C. Herring, Surface tension as a motivation for sintering, in *Fundamental Contributions to the Continuum Theory of Evolving Phase Interfaces in Solids*, edited by J. M. Ball, D. Kinderlehrer, P. Podio-Guidugli, and M. Slemrod (Springer, Berlin, Heidelberg, 1999), pp. 33–69.

[60] E. Bonnetier, E. Bretin, and A. Chambolle, Consistency result for a non monotone scheme for anisotropic mean curvature flow, Interfaces Free Bound. **14**, 1 (2012).

[61] M. Elsey and S. Esedoḡlu, Threshold dynamics for anisotropic surface energies, Math. Comput. **87**, 1721 (2018).

[62] S. Esedoḡlu and M. Jacobs, Convolution kernels and stability of threshold dynamics methods, SIAM J. Numer. Anal. **55**, 2123 (2017).

[63] S. Esedoḡlu, M. Jacobs, and P. Zhang, Kernels with prescribed surface tension & mobility for threshold dynamics schemes, J. Comput. Phys. **337**, 62 (2017).

[64] H. Ishii, G. E. Pires, and P. E. Souganidis, Threshold dynamics type approximation schemes for propagating fronts, J. Math. Soc. Jpn. **51**, 267 (1999).

[65] D. L. Olmsted, S. M. Foiles, and E. A. Holm, Survey of computed grain boundary properties in face-centered cubic metals: I. Grain boundary energy, Acta Mater. **57**, 3694 (2009).

[66] G. S. Rohrer, E. A. Holm, A. D. Rollett, S. M. Foiles, J. Li, and D. L. Olmsted, Comparing calculated and measured grain boundary energies in nickel, Acta Mater. **58**, 5063 (2010).

[67] B. Merriman and S. J. Ruuth, Convolution-generated motion and generalized Huygens' principles for interface motion, SIAM J. Appl. Math. **60**, 868 (2000).

[68] W. T. Read and W. Shockley, Dislocation models of crystal grain boundaries, Phys. Rev. **78**, 275 (1950).

[69] X. Peng, Computational methods for structure-property relations in heterogeneous materials, Ph.D. thesis, Carnegie Mellon University, 2021.

[70] M. A. Groeber and M. A. Jackson, DREAM.3D: A digital representation environment for the analysis of microstructure in 3D, Integr. Mater. Manuf. Innov. **3**, 56 (2014).

[71] V. Mohles, 3-D front tracking model for interfaces with anisotropic energy, Comput. Mater. Sci. **176**, 109534 (2020).

[72] G. S. Rohrer, I. Chesser, A. R. Krause, S. K. Naghibzadeh, Z. Xu, K. Dayal, and E. A. Holm, Grain boundary migration in polycrystals, Annu. Rev. Mater. Res. **53**, 347 (2023).

[73] C. M. Hefferan, Measurement of annealing phenomena in high purity metals with near-field high energy x-ray diffraction microscopy, Ph.D. thesis, Carnegie Mellon University, 2012.

[74] C. M. Hefferan, S. F. Li, J. Lind, and R. M. Suter, Tests of microstructure reconstruction by forward modeling of high

energy x-ray diffraction microscopy data, Powder Diffr. **25**, 132 (2010).

[75] S. F. F. Li, Imaging of orientation and geometry in microstructures: development and applications of high energy x-ray diffraction microscopy, Ph.D. thesis, Carnegie Mellon University, 2011.

[76] K. Glowinski and A. Morawiec, Analysis of experimental grain boundary distributions based on boundary-space metrics, Metall. Mater. Trans. A **45**, 3189 (2014).

[77] X. Zhong, D. J. Rowenhorst, H. Beladi, and G. S. Rohrer, The five-parameter grain boundary curvature distribution in an austenitic and ferritic steel, Acta Mater. **123**, 136 (2017).

[78] J. Zhang, Y. Zhang, W. Ludwig, D. Rowenhorst, P. W. Voorhees, and H. F. Poulsen, Three-dimensional grain growth in pure iron. Part I. Statistics on the grain level, Acta Mater. **156**, 76 (2018).

[79] A. Qiu, I. Chesser, and E. Holm, On the variability of grain boundary mobility in the isoconfigurational ensemble, Acta Mater. **257**, 119075 (2023).

[80] O. Chirayutthanasak, R. Sarochawikasit, S. Khongpia, T. Okita, S. Dangtip, G. S. Rohrer, and S. Ratanaphan, Universal function for grain boundary energies in bcc metals, Scr. Mater. **240**, 115821 (2024).

[81] https://github.com/Kiana-Naghibzadeh/TD_aniso_BRK.

[82] http://mimp.materials.cmu.edu/~gr20/Grain_Boundary_Data_Archive/Ni_velocity/Ni_velocity.html.